

www.acsaem.org

Article

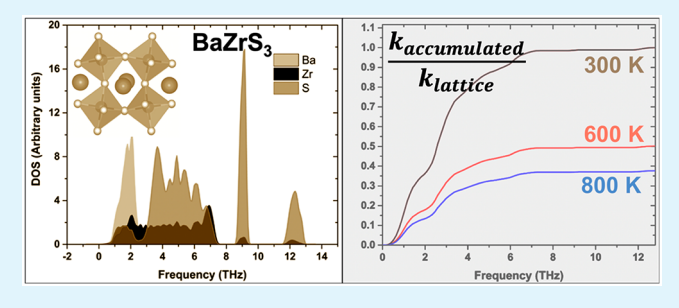
Understanding the Extremely Poor Lattice Thermal Transport in Chalcogenide Perovskite BaZrS₃

Eric Osei-Agyemang and Ganesh Balasubramanian*

Department of Mechanical Engineering and Mechanics, Lehigh University, 19 Memorial Drive West, Bethlehem, Pennsylvania 18015, United States

Supporting Information

ABSTRACT: Combining first-principles calculations with the solution to the Boltzmann transport equations, we examine the lattice thermal transport for the orthorhombic perovskite BaZrS₃ through analyses of phonon group velocities, lifetimes, average Grüneisen parameter, and Debye temperature. An extremely low lattice thermal conductivity (LTC) of 1.16 Wm⁻¹ K⁻¹ at 300 K is obtained with phonons at 0-4 THz being the main contributors. The acoustic phonons contribute ~30% to the LTC, while the lower frequency range of the optical modes contributes the most. Nearly 83% of the



accumulated LTC is contributed by phonons with MFP < 5 nm. Since the lattice parameter (9.98 Å) of BaZrS₃ is not significantly different from the calculated MFP, we corroborate that nanostructuring might be ineffective to reduce LTC.

KEYWORDS: chalcogenide perovskite, BaZrS₃₁, phonon dispersion, density of states, lattice conductivity, thermoelectrics

1. INTRODUCTION

The search for thermoelectrics with low lattice thermal conductivity (LTC) and an optimum figure of merit that are comparable in power conversion efficiency and performance to commercially available materials such as CuInSe2 and CdTe is ongoing. 1-3 Though organic-inorganic halide perovskites such as methylammonium lead iodide (MAPbI₃) and methylammonium tin iodide (MAPbSn₃) hold promise, the presence of toxic elements, such as lead, renders them less suitable for environmentally friendly applications.^{4–11} On the other hand, chalcogenide perovskites in the distorted orthorhombic phase with the ABX₃ structure have been found to possess good optical properties, ^{12,13} power conversion factors, and thermoelectric performance that is comparable to traditional thermoelectric materials. 14 Recent interests in chalcogenide perovskites have focused on the structural characterization, 15 electronic band gap, and optical absorption properties. Nevertheless, LTC ($\kappa_{\rm L}$) plays an important role as materials with a high κ_L contribute to an enhanced heat rejection from the electronic devices, but simultaneously decrease their potential of being good thermoelectrics. For nonmetallic crystals to possess low LTC, the requirements include weak interatomic bonding interactions, the presence of heavy elements, structural complexity, and large Grüneisen parameters.²² Here, we examine phonon transport through a representative chalcogenide perovskite, barium zirconium sulfide (BaZrS₃, a.k.a., BZS), and correlate its LTC predictions to corresponding analyses of phonon dispersion, phonon group velocities, Grüneisen parameters, and phonon lifetimes using the Boltzmann transport equation. As discussed below in detail,

strong anharmonicity, low phonon number density in the acoustic region, and low phonon lifetimes all contribute to a very low $\kappa_L = 1.16 \text{ Wm}^{-1} \text{ K}^{-1}$ at 300 K. The structure for the distorted orthorhombic BaZrS3 employed here is illustrated in Figure 1. The structure is composed of corner-sharing perovskite structures (Zr at the center and S atoms at the sharing corners) with Ba atoms sitting at the hollow sites within the perovskite framework.

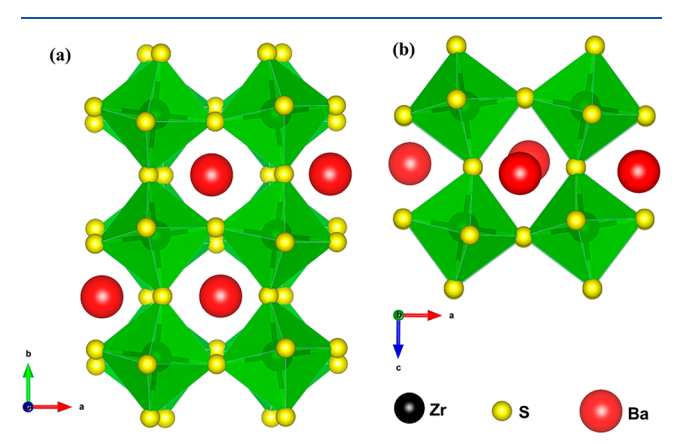


Figure 1. Distorted perovskite structure of BaZrS₃. (a) Side view and (b) top view.

Received: November 7, 2019 Accepted: December 6, 2019 Published: December 6, 2019



ACS Applied Energy Materials

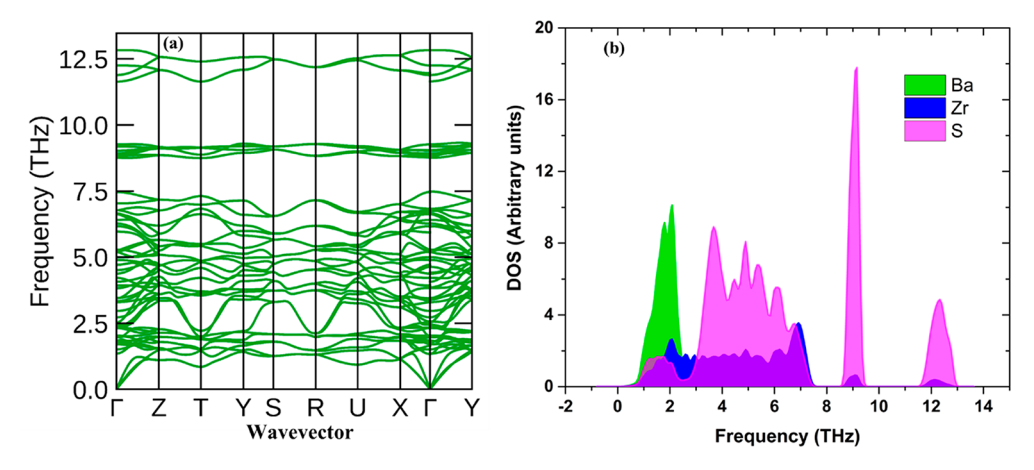


Figure 2. (a) Phonon dispersion and (b) phonon density of states for BaZrS₃ in the distorted orthorhombic perovskite phase.

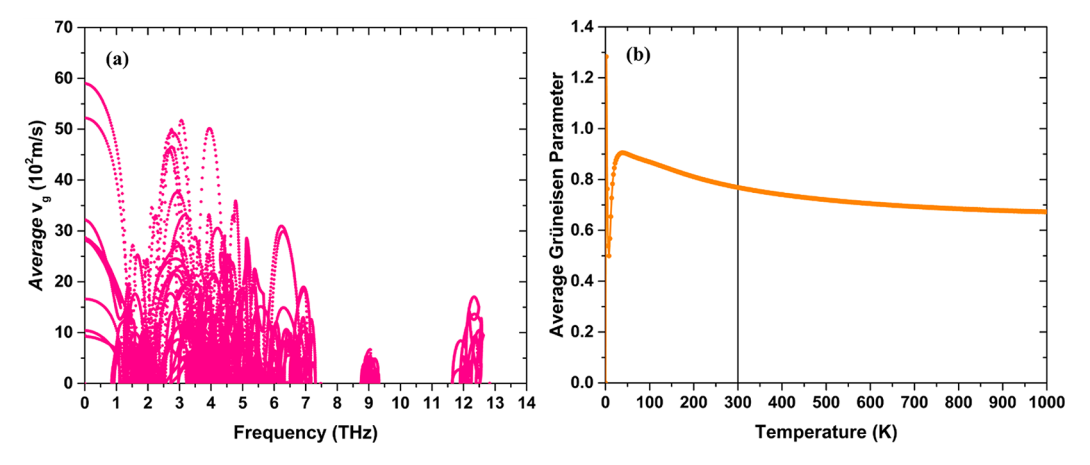


Figure 3. (a) Average phonon group velocity and (b) average Grüneisen parameter for BaZrS₃. The vertical line in (b) denotes the average Grüneisen parameter at 300 K.

2. RESULTS AND DISCUSSION

The calculated phonon dispersion and phonon density of states (DOS) for BaZrS₃ are presented in Figure 2. The absence of negative frequency phonon modes demonstrates the dynamic stability of the BaZrS₃ orthorhombic perovskite phase.

Among the 60 phonon modes, the three acoustic modes (LA, TA, and ZA) exist in the lowest frequency regime with the highest acoustic frequency at 1.5 THz. The remaining phonon modes are the optical modes with the highest phonon vibrational frequency occurring at 13 THz. There is no clear phonon band gap between the acoustic and the optical phonon modes. However, gaps exist in the upper zones of the optical phonon region. From Figure 2(b), we note that the lower part of the optical modes (2–8 THz) is dispersive and that these branches are expected to contribute significantly to the LTC of BaZrS₃. The coupling of the acoustic modes with the lower section of the optical modes leads to the latter affecting κ_L . However, the upper region of the optical modes being localized, they are effective in reducing the LTC.

The average phonon group velocities and Grüneisen parameters are shown in Figure 3. The highest phonon group velocities are recorded for the acoustic phonon modes (<1 THz). Phonon group velocities for the lower region of the optical modes are also significantly high. However, the low phonon number density in the acoustic region indicates a low LTC since the acoustic modes are expected to exert the

highest contribution to κ_L . Thus, we anticipate LTC predictions for BaZrS₃ to yield low κ_L values.

The average Grüneisen parameter is used to characterize the anharmonicity in the BaZrS3 crystal. According to the Slack's model²² for $\kappa_{\rm L} = \frac{A\bar{M}\Theta_{\rm D}\delta^{1/3}N^{1/3}}{\gamma^2T}$, the LTC is inversely proportional to the square of the average Grüneisen parameter γ . Here, A is a constant, \overline{M} is the average atomic mass, $\Theta_{\rm D}$ is the Debye temperature, T is temperature, δ is volume per atom, and N is the number of atoms per unit cell. A higher Grüneisen parameter of a crystal indicates higher lattice anharmonic effects in the phonon spectrum due to the change of cell volume, and this typically leads to a lower LTC. As noted above from the equation for Slack's model, strong anharmonicity that is indicative of a higher Grüneisen parameter leads to a lower LTC value. The Grüneisen parameter, defined as the change of the vibrational frequency of a given mode with volume, $\gamma = -\frac{\mathrm{d}(\ln \omega_i)}{\mathrm{d}(\ln V)}$, is a function of the volume V. However, γ determined from the thermal expansion data averages over all phonon modes including the optical branches, as presented in Figure 3(b). An estimated Grüneisen parameter of ~0.8 is obtained at 300 K; this relatively high γ is hence expected to result in a low LTC for BaZrS₃. Though the estimated γ value is lower than that obtained for PbTe $(1.65)^{23}$ and SnSe $(3.13)^{23}$ it is considered relatively high and expected to result in a low LTC value.

ACS Applied Energy Materials

The LTC is directly proportional to the phonon lifetimes. Hence, we illustrate the calculated lifetimes at different frequencies in Figure 4. The phonon modes are represented as

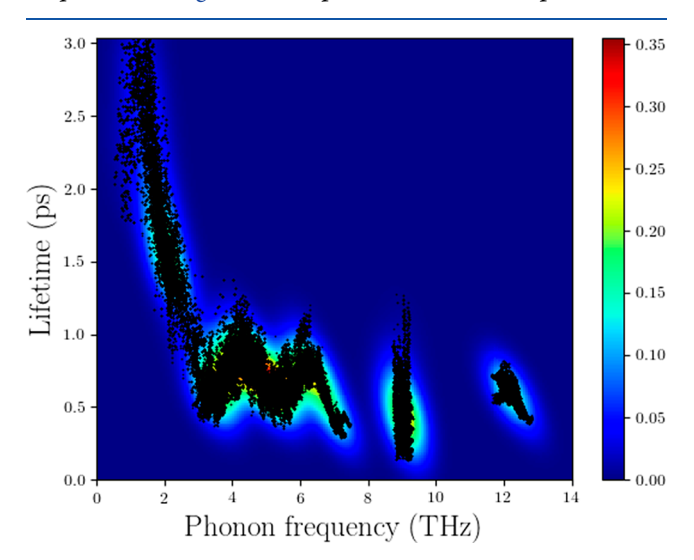


Figure 4. Phonon lifetime as a function of the phonon frequency for BaZrS₃ calculated at 300 K. Four different groups of phonon modes are observed that corroborate with the predictions from the DOS in Figure 2(b).

black dots over a colored background with the region of highest phonon mode density being represented in red or orange. From 0 THz onward, the phonon lifetime decreases rapidly as frequency increases with an intermediate rise and drops between 3 THz and 7 THz. From 7 to 13 THz, the average phonon lifetime remains fairly constant at ~ 0.65 ps. The distribution of phonon lifetimes reveals that the distorted orthorhombic perovskite possesses low phonon lifetimes with the highest phonon lifetime observed at ~3 ps compared to PbTe which has a higher phonon lifetime of ~8 ps.²⁴ Since these phonons in BaZrS3 have extremely short lifetimes, the phonon-phonon scattering rates are significantly increased, thereby reducing the LTC. The highest phonon lifetimes are noted between 0 THz and 3 THz. The phonon groups are centered between 1 and 2 THz, 3-7 THz, 9 THz, and 12.5 THz which agrees well with the phonon DOS discussed earlier in Figure 2(b) (where the highest peaks occurring at 1-2, 3-7, 9, and 12.5 THz exactly coincides with the cluster centroids in Figure 4). Due to the many phonon modes that exists at these centroids (red or orange backgrounds), the significant phonon-phonon scattering or Umklapp processes occurring in these regions subsequently leads to phonon annihilation.

The optical phonons that exists between frequencies of 8-13 THz have short phonon lifetimes due to enhanced phonon-phonon scattering and contribute to impeding the phonon thermal transport with increasing temperatures as can be seen from the constant profile of the phonon lifetimes between 8 and 13 THz. Phonons in the lower portion of the optical branches between 3 and 7 THz also possess low phonon lifetimes, and there is only a marginal decrease in the phonon lifetimes when shifting from 3 to 7 THz which leads to lower contribution to the LTC as can be noted later from Figure 7(a) (25% contribution to LTC). The phonon modes that have relatively longer lifetimes and expected to constructively influence the LTC are the acoustic modes

(0-1 THz) and some lower optical modes (1-2 THz). However, the phonon number density in the acoustic region results in a reduced LTC. The acoustic-optical mode coupling is reflected from the phonon lifetimes in Figure 4 as continuous black dots between 1 and 2 THz. The calculated heat capacity at constant pressure (C_n) at different temperatures is shown in Figure 5. The Dulong-Petit limit

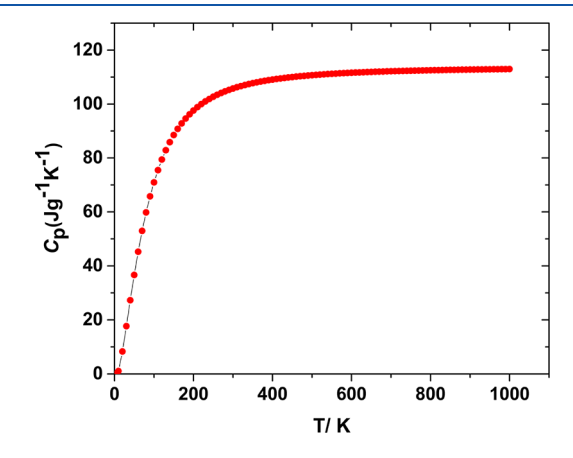


Figure 5. Heat capacity at constant pressure C_p at different temperatures for BaZrS3 in the orthorhombic-distorted perovskite phase.

for the heat capacity is observed around 400 K. We also anticipate a somewhat higher Debye temperature of around 400 K for $BaZrS_3$ as compared to 142 K for SnSe, 164 K for PbTe, 190 K for PbSe, and 213 K for PbS.²

The Debye temperatures for SnSe, PbSe, PbTe, and PbS are

calculated from the average speed of sound through the lattice using the relation $\theta_{\rm D} = \frac{h}{k_{\rm B}} \left[\frac{3N}{4\pi V} \right]^{1/3} \nu_{\rm a}$, where h is Planck's constant, $k_{\rm B}$ is the Boltzmann constant, N is the number of atoms in a unit cell, V is the unit-cell volume, and v_a is the average sound velocity.²³ The calculated LTC of BaZrS₃ at different temperatures is shown in Figure 6. The κ_L value decreases rapidly from 10 to 200 K and plateaus at around 600 K. Though the LTC is calculated using the single-mode relaxation time approximation (RTA) method, it has been found to give accurate results as the difference between the RTA method and the iterative full solution is only noticeable for high LTC materials.²⁵ We predict that at 300 K $\kappa_L = 1.2$ Wm⁻¹ K⁻¹. The calculated LTC for BaZrS₃ is slightly higher than that calculated for SnSe (0.62 Wm⁻¹ K⁻¹) but lower than those for PbTe $(2.30 \text{ Wm}^{-1} \text{ K}^{-1})$ and PbSe $(2.64 \text{ Wm}^{-1} \text{ K}^{-1})$. As elaborated in the preceding discussions, this low LTC is attributed to the low number of phonons with significant phonon group velocities, strong anharmonicity, and low phonon lifetimes due to strong phonon-phonon scattering in BaZrS₃. However, the anisotropic effect in the calculated κ_L values is negligible across all temperatures. As presented in the inset of Figure 6, the calculated LTC values are marginally higher along the lattice Y-direction and lower along the Zdirection though the difference is insignificant. The description of the directions with regards to the crystallographic geometry are discussed in the Methods section below.

To analyze the contribution of different phonon modes to $\kappa_{\rm L}$, we calculate the accumulated LTC ($\kappa_{\rm a}$) at different frequencies of the phonon modes (Figure 7) as a function of temperature. The variable κ_a is normalized by the correspond**ACS Applied Energy Materials**

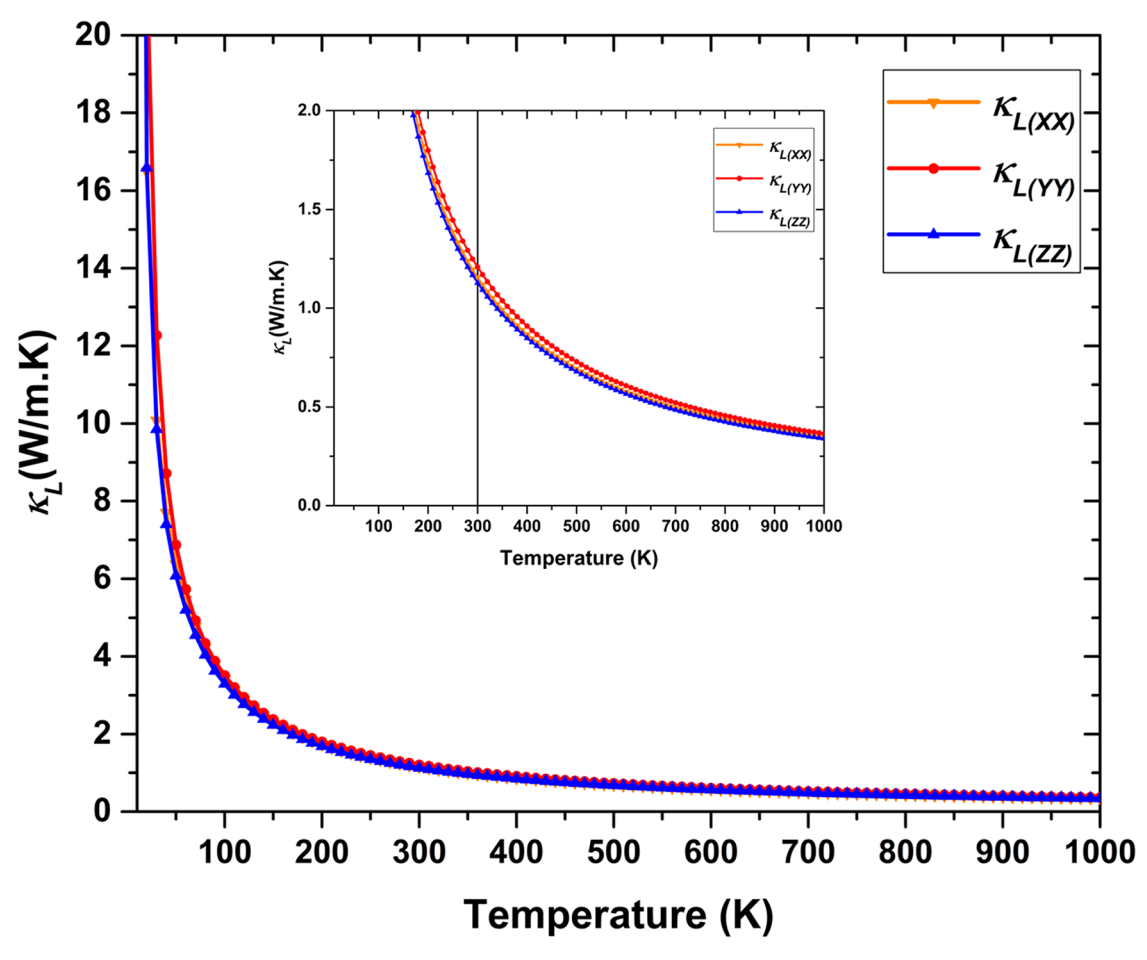


Figure 6. Lattice thermal conductivity (LTC) of BaZrS₃ at different temperatures along the three different crystallographic axes. The inset, a magnified section of the LTC, shows the lack of anisotropic effect for κ_L of BaZrS₃. The vertical line in the inset is the LTC at 300 K ($\kappa_L = 1.20$ W/m K).

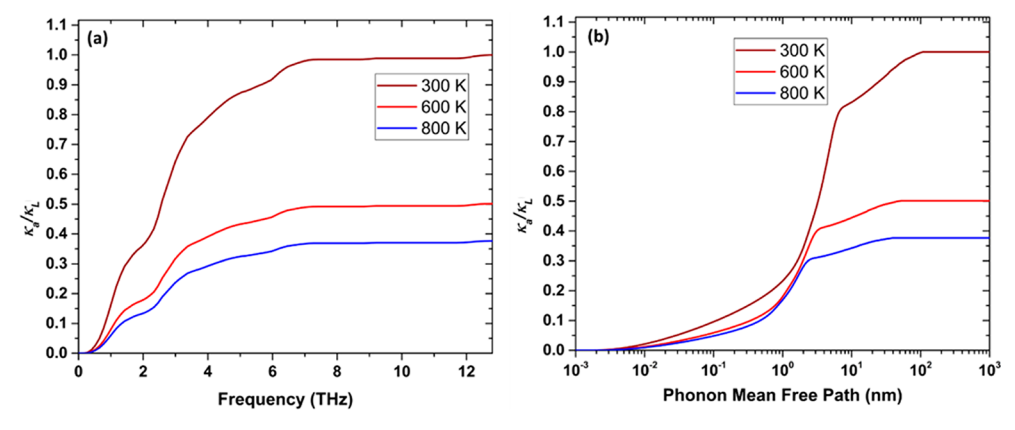


Figure 7. Accumulated lattice thermal conductivity for BaZrS₃ at different temperatures as a function of (a) frequency and (b) phonon mean free path.

ing κ_L predictions. From Figure 7(a), the acoustic phonon modes (0-1 THz) contribute ~30% to κ_a , while the optical modes in the 1.5-6 THz range contribute \sim 70%. Effectively, phonon modes with frequencies between 0 and 4 THz contribute 83% to the LTC, while phonons with frequencies of 4–6 THz account for ~17% to $\kappa_{\rm L}$. From 300 to 600 K, $\kappa_{\rm a}$ is reduced by 50%, while from 600 to 800 K the reduction is a further $\sim 50\%$.

In Figure 7(b), the distribution of κ_a against the logarithm of the phonon mean free path (MFP) shows the dependence

of the LTC on the size of the BaZrS₃ sample. κ_a attains its highest value when the sample size is equal to or greater than the largest phonon MFP. Thus, the calculated maximum phonon MFP can aid in designing nanostructured materials such that the LTC can be reduced to yield good thermo-electric properties.^{26–28} From Figure 7(b), it is apparent that phonons with MFP less than 3 nm contribute to 50% of the accumulated LTC. Moreover, about 85% of the accumulated LTC is contributed by phonons with an average MFP of 5 nm or less. The shorter MFP for the phonons leads to the lower

LTC values calculated for BaZrS₃. The calculated MFP of ~5 nm is comparable to the lattice parameter of BaZrS₃ (9.98 $\rm \AA)^{29}$ but much lower than the average MFP for SnSe (84 nm)²³ and PbTe (310 nm).²³ This observation corroborates the significantly lower LTC of BaZrS₃ compared to SnSe and PbTe. As the lattice parameter of BaZrS₃ is not considerably different from the calculated MFP, we assert that nanostructuring will be ineffective to further reduce the LTC, limiting the thermoelectric potential of BaZrS₃.

3. SUMMARY AND CONCLUSION

We examine the lattice thermal transport through orthorhombic perovskite BaZrS₃ by analyzing the phonon group velocities, phonon lifetimes, and average Grüneisen parameter. We predict that strong anharmonicity, low phonon number density in the acoustic region, and low phonon lifetimes all contribute to a very low room temperature $\kappa_{\rm L} = 1.16~{\rm Wm}^{-1}$ K⁻¹ for BaZrS₃. The phonons with frequencies from 0 to 4 THz are the main contributors to the LTC; however, the acoustic phonons contribute ~30%, while the lower frequency optical phonons that are coupled to the acoustic modes significantly impact the LTC of BaZrS3. Along the different crystallographic directions, we note negligible anisotropy in the LTC for this orthorhombic perovskite. The effect of the phonon mean free path (MFP) to the LTC is examined, and about 83% of the accumulated LTC is contributed by phonons with MFP < 5 nm.

4. METHODS

The projector augmented wave method (PAW)30 within the framework of density functional theory (DFT) as implemented in the VASP³¹ code is used for all first-principles calculations. The unit cell and atomic positions are relaxed using the PBEsol32 functional for solids, while the Methfessel-Paxton³³ smearing scheme is utilized with the gamma parameter set to 0.1 eV. An energy cutoff of 600 eV is used for the planewaves expansion. A Monkhorst-Pack³⁴ special grid sampling of the k-points for integration of the Brillouin zone yields 7 × 5 × 7 k-points representing 123 irreducible sampling points for all bulk calculations. Resolution of the Kohn-Sham equations is achieved by using the self-consistent field procedure and setting energy changes for each cycle at 10⁻⁴ eV as the convergence criterion between two successive iterations. The calculated lattice parameters in the a, b, and c directions are 7.066, 9.923, and 6.972 Å, respectively (Figure 1), in agreement with experimentally measured values of 7.060, 9.980, and 7.030 Å along the same directions.²

In calculating the atomic forces, we minimized the total forces until the energy convergence was less than 10^{-8} eV. The Born effective charge tensors and the static dielectric constant tensors are calculated using density functional perturbation theory as implemented in the VASP code, 35,36 and the tensors are symmetrized by their space-group and point-group operations. The calculated dielectric constants for the xx, yy, and zz components (corresponding to those along the a, b, and c directions) of the tensor are 10.372, 9.940, and 9.941, respectively, while the Born effective charges for the independent species are as follows: Ba (2.722, 2.707, and 2.750), Zr (8.158, 8.065, and 7.910), S_1 (-1.980, -6.406, and -2.242), and S_2 (-4.450, -2.183, and -4.210). Lattice thermal conductivity is calculated from $\kappa_{\rm L} = \frac{1}{NV_0} \sum_{\zeta} C_{\zeta} v_{\zeta} \otimes v_{\zeta} \tau_{\zeta}^{\rm RTA}$, where N is the number of unit cells in the crystal, V_0 is the volume of the unit cell, ν_ζ is the group velocity, $\tau_\zeta^{\rm RTA}$ is the relaxation time of the phonon mode ζ , and C_{ζ} is the mode-dependent heat capacity.

The phonon dispersion, phonon group velocities, and Grüneisen parameters are calculated using the PHONOPY³⁷ code with a qpoint sampling mesh of 21 × 21 × 21. The linearized phonon Boltzmann transport equation is solved under the single-mode relaxation time approximation (RTA) for calculating the LTC using

the $PHONO3PY^{38}$ code. Within the RTA approximation for calculating the LTC, we tested the convergence of the q-point sampling mesh (= $q \times q \times q$) with different q values and found that q = 13 to yield converged results. The q-convergence test results are provided in Figure S1 of the Supporting Information. The supercell approach was used to calculate the second- and third-order force constants by utilizing the finite displacement method; a $2 \times 2 \times 2$ supercell (160 atoms) and a $2 \times 1 \times 2$ supercell (80 atoms) of the unit cell are used for the calculation of the second-order and thirdorder force constants, respectively. Since computing the third-order force constants is the most computationally intensive and a consideration of all three-atom interactions results in tens of thousands of calculations, we used an interaction cutoff to reduce the number of force constant calculations. We used an interaction distance of up to the fourth-nearest neighbors for the three-atom interactions that reduces the number of force constant calculations to 1157. We apply a nonanalytical term correction to the dynamical matrix that is needed to treat the long-range dipole—dipole interactions. ^{39–41} The average phonon group velocities are calculated as the trace of the x, y, and z components of group velocity vector. In calculating the average Grüneisen parameter, three separate calculations are used where one is calculated at the equilibrium volume and the remaining two at slightly larger and smaller volumes under the constraint of each volume. The average Grüneisen parameter is then estimated as the change in vibrational frequency with volume using the quasi-harmonic approximation.

ASSOCIATED CONTENT

S Supporting Information

The Supporting Information is available free of charge at https://pubs.acs.org/doi/10.1021/acsaem.9b02185.

Result demonstrating the convergence test and selection of the sampling mesh employed for the first-principles calculations (PDF)

AUTHOR INFORMATION

Corresponding Author

*E-mail: bganesh@lehigh.edu. Tel.: +1 610 758 3784.

Ganesh Balasubramanian: 0000-0003-1834-5501

Author Contributions

E.O.-A. designed the project, performed all the calculations, and analyzed the results. G.B. conceived the idea. E.O.-A. and G.B. wrote the manuscript.

Notes

The authors declare no competing financial interest.

ACKNOWLEDGMENTS

This work was supported, in part, by the National Science Foundation (NSF) through award CMMI-1753770. The computations were carried out on the cluster Sol managed by the Library and Technology Services Research Computing at Lehigh University. The authors thank Challen Enninful Adu for assistance with executing some of the computations.

REFERENCES

- (1) Park, N.-G. Organometal Perovskite Light Absorbers Toward a 20% Efficiency Low-Cost Solid-State Mesoscopic Solar Cell. J. Phys. Chem. Lett. 2013, 4 (15), 2423-2429.
- (2) Bisquert, J. The Swift Surge of Perovskite Photovoltaics. J. Phys. Chem. Lett. 2013, 4 (15), 2597-2598.
- (3) Chen, Q.; De Marco, N.; Yang, Y. M.; Song, T.-B.; Chen, C.-C.; Zhao, H.; Hong, Z.; Zhou, H.; Yang, Y. Under the Spotlight: The Organic-Inorganic Hybrid Halide Perovskite for Optoelectronic Applications. Nano Today 2015, 10 (3), 355-396.

- (4) Repins, I.; Contreras, M. A.; Egaas, B.; DeHart, C.; Scharf, J.; Perkins, C. L.; To, B.; Noufi, R. 19-9%-Efficient ZnO/CdS/ CuInGaSe2 Solar Cell with 81.2% Fill Factor. Prog. Photovoltaics 2008, 16 (3), 235-239.
- (5) Snaith, H. J. Perovskites: The Emergence of a New Era for Low-Cost, High-Efficiency Solar Cells. J. Phys. Chem. Lett. 2013, 4 (21), 3623-3630.
- (6) Zhou, H.; Chen, Q.; Li, G.; Luo, S.; Song, T.; Duan, H.-S.; Hong, Z.; You, J.; Liu, Y.; Yang, Y. Interface Engineering of Highly Efficient Perovskite Solar Cells. Science 2014, 345 (6196), 542-546.
- (7) Burschka, J.; Pellet, N.; Moon, S.-J.; Humphry-Baker, R.; Gao, P.; Nazeeruddin, M. K.; Grätzel, M. Sequential Deposition as a Route to High-Performance Perovskite-Sensitized Solar Cells. Nature 2013, 499 (7458), 316-319.
- (8) Singh, R.; Balasubramanian, G. Impeding Phonon Transport through Superlattices of Organic-Inorganic Halide Perovskites. RSC Adv. 2017, 7 (59), 37015-37020.
- (9) Leijtens, T.; Eperon, G. E.; Pathak, S.; Abate, A.; Lee, M. M.; Snaith, H. J. Overcoming Ultraviolet Light Instability of Sensitized TiO2 with Meso-Superstructured Organometal Tri-Halide Perovskite Solar Cells. Nat. Commun. 2013, 4, 2885.
- (10) Noh, J. H.; Im, S. H.; Heo, J. H.; Mandal, T. N.; Seok, S. I. Chemical Management for Colorful, Efficient, and Stable Inorganic-Organic Hybrid Nanostructured Solar Cells. Nano Lett. 2013, 13 (4), 1764-1769.
- (11) Christians, J. A.; Miranda Herrera, P. A.; Kamat, P. V. Transformation of the Excited State and Photovoltaic Efficiency of CH3NH3PbI3 Perovskite upon Controlled Exposure to Humidified Air. J. Am. Chem. Soc. 2015, 137 (4), 1530-1538.
- (12) Grinberg, I.; West, D. V.; Torres, M.; Gou, G.; Stein, D. M.; Wu, L.; Chen, G.; Gallo, E. M.; Akbashev, A. R.; Davies, P. K.; Spanier, J. E.; Rappe, A. M. Perovskite Oxides for Visible-Light-Absorbing Ferroelectric and Photovoltaic Materials. Nature 2013, 503 (7477), 509-512.
- (13) Swarnkar, A.; Mir, W. J.; Chakraborty, R.; Jagadeeswararao, M.; Sheikh, T.; Nag, A. Are Chalcogenide Perovskites an Emerging Class of Semiconductors for Optoelectronic Properties and Solar Cell? Chem. Mater. 2019, 31 (3), 565-575.
- (14) Osei-Agyemang, E.; Enninful Adu, C.; Balasubramanian, G. Doping and Anisotropy-Dependent Electronic Transport in Chalcogenide Perovskite CaZrSe₃ for High Thermoelectric Efficiency. Advanced Theory and Simulations 2019, 2 (9), 1900060.
- (15) Niu, S.; Zhao, B.; Ye, K.; Bianco, E.; Zhou, J.; McConney, M. E.; Settens, C.; Haiges, R.; Jaramillo, R.; Ravichandran, J. Crystal Growth and Structural Analysis of Perovskite Chalcogenide BaZrS₃ and Ruddlesden-Popper Phase Ba₃Zr₂S₇. J. Mater. Res. 2019, 34,
- (16) Lee, C.-S.; Kleinke, K. M.; Kleinke, H. Synthesis, Structure, and Electronic and Physical Properties of the Two SrZrS3 Modifications. Solid State Sci. 2005, 7 (9), 1049-1054.
- (17) Sun, Y.-Y.; Agiorgousis, M. L.; Zhang, P.; Zhang, S. Chalcogenide Perovskites for Photovoltaics. Nano Lett. 2015, 15 (1), 581-585.
- (18) Gross, N.; Sun, Y.-Y.; Perera, S.; Hui, H.; Wei, X.; Zhang, S.; Zeng, H.; Weinstein, B. A. Stability and Band-Gap Tuning of the Chalcogenide Perovskite BaZrS3 in Raman and Optical Investigations at High Pressures. Phys. Rev. Appl. 2017, 8 (4), 044014.
- (19) Bennett, J. W.; Grinberg, I.; Rappe, A. M. Effect of Substituting of S for O: The Sulfide Perovskite BaZrS₃ Investigated with Density Functional Theory. Phys. Rev. B: Condens. Matter Mater. Phys. 2009, 79 (23), 235115.
- (20) Niu, S.; Huyan, H.; Liu, Y.; Yeung, M.; Ye, K.; Blankemeier, L.; Orvis, T.; Sarkar, D.; Singh, D. J.; Kapadia, R.; Ravichandran, J. Bandgap Control via Structural and Chemical Tuning of Transition Metal Perovskite Chalcogenides. Adv. Mater. 2017, 29 (9), 1604733.
- (21) Niu, S.; Joe, G.; Zhao, H.; Zhou, Y.; Orvis, T.; Huyan, H.; Salman, J.; Mahalingam, K.; Urwin, B.; Wu, J.; Liu, Y.; Tiwald, T. E.; Cronin, S. B.; Howe, B. M.; Mecklenburg, M.; Haiges, R.; Singh, D. J.; Wang, H.; Kats, M. A.; Ravichandran, J. Giant Optical Anisotropy

- in a Quasi-One-Dimensional Crystal. Nat. Photonics 2018, 12 (7), 392-396.
- (22) Slack, G. A. Nonmetallic Crystals with High Thermal Conductivity. J. Phys. Chem. Solids 1973, 34 (2), 321-335.
- (23) Xiao, Y.; Chang, C.; Pei, Y.; Wu, D.; Peng, K.; Zhou, X.; Gong, S.; He, J.; Zhang, Y.; Zeng, Z.; Zhao, L. Origin of Low Thermal Conductivity in SnSe. Phys. Rev. B: Condens. Matter Mater. Phys. 2016, 94 (12), 125203.
- (24) Lu, Y.; Sun, T.; Zhang, D.-B. Lattice Anharmonicity, Phonon Dispersion, and Thermal Conductivity of PbTe Studied by the Phonon Quasiparticle Approach. Phys. Rev. B: Condens. Matter Mater. Phys. 2018, 97 (17), 174304.
- (25) Shafique, A.; Samad, A.; Shin, Y.-H. Ultra Low Lattice Thermal Conductivity and High Carrier Mobility of Monolayer SnS₂ and SnSe2: A First Principles Study. Phys. Chem. Chem. Phys. 2017, 19 (31), 20677-20683.
- (26) Balandin, A.; Wang, K. L. Significant Decrease of the Lattice Thermal Conductivity Due to Phonon Confinement in a Free-Standing Semiconductor Quantum Well. Phys. Rev. B: Condens. Matter Mater. Phys. 1998, 58 (3), 1544-1549.
- (27) Aketo, D.; Shiga, T.; Shiomi, J. Scaling Laws of Cumulative Thermal Conductivity for Short and Long Phonon Mean Free Paths. Appl. Phys. Lett. 2014, 105 (13), 131901.
- (28) Fugallo, G.; Cepellotti, A.; Paulatto, L.; Lazzeri, M.; Marzari, N.; Mauri, F. Thermal Conductivity of Graphene and Graphite: Collective Excitations and Mean Free Paths. Nano Lett. 2014, 14 (11), 6109-6114.
- (29) Lelieveld, R.; Ijdo, D. J. W. Sulphides with the GdFeO 3 Structure. Acta Crystallogr., Sect. B: Struct. Crystallogr. Cryst. Chem. 1980, 36 (10), 2223-2226.
- (30) Kresse, G.; Joubert, D. From Ultrasoft Pseudopotentials to the Projector Augmented-Wave Method. Phys. Rev. B: Condens. Matter Mater. Phys. 1999, 59 (3), 1758-1775.
- (31) Hafner, J. Ab-Initio Simulations of Materials Using VASP: Density-Functional Theory and Beyond. J. Comput. Chem. 2008, 29 (13), 2044-2078.
- (32) Perdew, J. P.; Ruzsinszky, A.; Csonka, G. I.; Vydrov, O. A.; Scuseria, G. E.; Constantin, L. A.; Zhou, X.; Burke, K. Restoring the Density-Gradient Expansion for Exchange in Solids and Surfaces. Phys. Rev. Lett. 2008, 100 (13), 136406.
- (33) Methfessel, M.; Paxton, A. T. High-Precision Sampling for Brillouin-Zone Integration in Metals. Phys. Rev. B: Condens. Matter Mater. Phys. 1989, 40 (6), 3616-3621.
- (34) Monkhorst, H. J.; Pack, J. D. Special Points for Brillouin-Zone Integrations. Phys. Rev. B 1976, 13 (12), 5188-5192.
- (35) Gajdoš, M.; Hummer, K.; Kresse, G.; Furthmüller, J.; Bechstedt, F. Linear Optical Properties in the Projector-Augmented Wave Methodology. Phys. Rev. B: Condens. Matter Mater. Phys. 2006, 73 (4), 045112.
- (36) Wu, X.; Vanderbilt, D.; Hamann, D. R. Systematic Treatment of Displacements, Strains, and Electric Fields in Density-Functional Perturbation Theory. Phys. Rev. B: Condens. Matter Mater. Phys. **2005**, 72 (3), 035105.
- (37) Togo, A.; Tanaka, I. First Principles Phonon Calculations in Materials Science. Scr. Mater. 2015, 108, 1-5.
- (38) Togo, A.; Chaput, L.; Tanaka, I. Distributions of Phonon Lifetimes in Brillouin Zones. Phys. Rev. B: Condens. Matter Mater. Phys. 2015, 91 (9), 094306.
- (39) Pick, R. M.; Cohen, M. H.; Martin, R. M. Microscopic Theory of Force Constants in the Adiabatic Approximation. Phys. Rev. B **1970**, 1 (2), 910–920.
- (40) Gonze, X.; Charlier, J.-C.; Allan, D. C.; Teter, M. P. Interatomic Force Constants from First Principles: The Case of α -Quartz. Phys. Rev. B: Condens. Matter Mater. Phys. 1994, 50 (17), 13035-13038.
- (41) Gonze, X.; Lee, C. Dynamical Matrices, Born Effective Charges, Dielectric Permittivity Tensors, and Interatomic Force Constants from Density-Functional Perturbation Theory. Phys. Rev. B: Condens. Matter Mater. Phys. 1997, 55 (16), 10355-10368.